

Article

Insight into Asymmetry in the Impact of Different Types of ENSO on the NAO

Peng Zhang and Zhiwei Wu *

Department of Atmospheric and Oceanic Sciences, Institute of Atmospheric Sciences, Shanghai Scientific Frontier Base of Ocean-Atmosphere Interaction, Fudan University, Shanghai 200438, China; zhang_peng@fudan.edu.cn

* Correspondence: zhiweiwu@fudan.edu.cn

Abstract: Understanding the influence of the El Niño–Southern Oscillation (ENSO) on the North Atlantic Oscillation (NAO) is of critical significance for seasonal prediction. The present study found that both Niño3.4 sea surface temperature anomaly (SSTA) intensity and east-west gradient in the mid-low latitude Pacific determine the linkage between ENSO and the NAO. Based on Niño3.4 SSTA intensity and the east-west gradient, ENSO events are classified into three types: strong intensity, weak intensity-strong gradient (WSG), and equatorial ENSOs. Note that the former two types are usually concurrent with a strong zonal SSTA gradient. In contrast, equatorial ENSO is often associated with weak intensity-weak gradient SSTAs confined in the equatorial Pacific. The anomalous circulation patterns in response to the three types of ENSO exhibit asymmetric features over the North Atlantic. The WSG-El Niño associated circulation anomaly resembles a negative NAO-like pattern, yet the strong and equatorial El Niño associated circulation anomalies show a neutral-NAO pattern. For La Niña events, their impact on the NAO mainly depends on the cold SSTA position rather than their intensity. The strong and WSG-La Niña associated negative SSTAs are centered in the equatorial-central Pacific and favor a steady positive NAO-like anomaly. The cold SSTA center of equatorial La Niña shifts to the equatorial-eastern Pacific and cannot profoundly influence the North Atlantic climate. The physical mechanisms are also investigated with a general circulation model.

Keywords: El Niño-southern oscillation; North Atlantic oscillation; asymmetry of ENSO



Citation: Zhang, P.; Wu, Z. Insight into Asymmetry in the Impact of Different Types of ENSO on the NAO. *Climate* **2023**, *11*, 136. <https://doi.org/10.3390/cli11070136>

Academic Editors: Xiaolei Zou, Guoxiong Wu and Zhemin Tan

Received: 23 May 2023
Revised: 22 June 2023
Accepted: 23 June 2023
Published: 27 June 2023



Copyright: © 2023 by the authors. Licensee MDPI, Basel, Switzerland. This article is an open access article distributed under the terms and conditions of the Creative Commons Attribution (CC BY) license (<https://creativecommons.org/licenses/by/4.0/>).

1. Introduction

As the prominent atmospheric mode occurring in the North Atlantic, the North Atlantic Oscillation (NAO) features an alternation of air mass over Iceland and the Azores [1–3]. Changes in the polarity and intensity of NAO exert profound influences on the surface air temperature and precipitation across the broad areas of North America and Eurasia [4]. In the positive phase, the pressure difference between the Icelandic Low and the Azores High is stronger than average, resulting in stronger westerly winds and storm tracks over the North Atlantic. This can lead to wetter and stormier conditions in Western Europe, while eastern parts may experience milder and drier weather. Conversely, the negative phase of the NAO exhibits almost the opposite characteristics. It is commonly recognized that the formation of NAO arises from the internal stochastic processes of the atmosphere [5,6]. One thing that has become clear is that the forcing stemming from the stratosphere [7–9] and sea surface temperature (SST) anomalies can also generate NAO-like anomalies [10–12].

The El Niño-Southern Oscillation (ENSO) is the dominant interannual air-sea coupled mode in the topics, which exerts salient impacts on global climate via localized forcing or remote teleconnections [13–17]. Whether the ENSO SSTA can excite the NAO-like atmospheric pattern or not, however, is still debated. Early research [18,19] believed that ENSO-related climate variability is hard to observe over the North Atlantic-Eurasia sectors. Despite the strong intrinsic variability of NAO, more and more observational and numerical

experimental evidence has proven that a negative NAO-like anomaly sometimes occurs in the El Niño winter; by contrast, a positive NAO-like pattern coincides with the La Niña events [20–22]. The ENSO-NAO relationship, therefore, may provide a potential source for seasonal climate prediction in North America and Eurasia [23]. Nevertheless, many studies also found that the atmospheric signals of ENSO over the North Atlantic exhibit salient inter-event variability [24–28]. This unstable behavior may be attributed to tropical volcanic eruptions, other non-ENSO factors [23,29], the interdecadal variation of ENSO itself [30], and the diversity of ENSO [24,26].

The ENSO diversity involves varying amplitudes and SSTA patterns [31]. The strong ENSOs with SSTAs larger in amplitude usually induced enormous property loss and casualties, grabbing the close attention of the scientific community [32,33]. However, a growing number of studies noticed the impact of moderate ENSOs, emphasizing that atmospheric responses to strong and moderate ENSOs sometimes show patterns with opposite signs rather than reduced amplitudes [27,34,35]. Diverse ENSO patterns have been apparent in recent decades when central Pacific (CP) ENSOs have occurred frequently, exerting impacts that differ from the conventional (eastern Pacific, EP) ENSO in terms of their disparate atmosphere-ocean coupling processes [36–39]. This classification, however, does not distinguish moderate ENSOs from strong ones, although strong El Niños usually exhibit an EP type, making it difficult to explain the climatic impact and evolution of relatively weak ENSOs. Wang et al. [40] classified El Niño events as strong basin-wide, moderate eastern Pacific, moderate central Pacific, and successive events. They revealed that the more frequent occurrence of extreme ENSOs in the past 40 years might be attributed to a background warming in the equatorial western Pacific and associated enhanced zonal SST gradients in the equatorial central Pacific.

The zonal SST gradients reflect the SSTA contrast between the western and eastern Pacific, which accelerates the equatorial zonal wind and increases the tilt of the thermocline, favoring the maintenance of an ENSO event [41]. As an indispensable segment of the Bjerknes positive feedback, zonal SSTA gradient largely furnishes violent tropic deep convections [42] and determines extratropical teleconnections [43–45]. Referencing Wang et al. [40], Zhang P et al. [27] classified ENSO events according to their amplitude and maximum SST, divided the winter La Niña events, based on the ENSO intensity and east-west gradient in the Pacific basin, into three groups: strong intensity La Niñas, weak intensity La Niñas with strong or weak gradients (their features are summarized in Table 1), and those impacted by the three flavors of La Niña on the East Asian winter monsoon. Whether or not El Niño events can be divided into three similar categories can be debated.

This study attempts to determine what types of El Niño and La Niña can profoundly impact NAO. Moreover, owing to the asymmetries that exist in amplitudes [46–48], evolutions [49–51], and effects [52,53], the warm and cold ENSOs, therefore, are not simply mirror images of each other. A systematic contrastive study of the physical process and mechanism for the impact of diverse warm and cold ENSO events on NAO is necessary. To discuss the above questions, Section 2 displays the datasets and model. Section 3 shows the diverse ENSOs and their impacts on NAOs. The possible mechanisms are discussed in Section 4. In Section 5, the major conclusions and discussions are exhibited.

Table 1. The years of different ENSO types.

Events	Years	Common Features
Strong El Niño	1957–1958, 1965–1966 , 1972–1973, 1982–1983, 1991–1992, 1997–1998, 2009–2010, 2015–2016 (8)	The strong warm (cool) SST anomalies in the eastern (western) Pacific with salient Indian Ocean warming
Strong La Niña	1970–1971, 1973–1974 , 1975–1976, 1988–1989 , 1998–1999, 1999–2000 , 2007–2008, 2010–2011 (8)	The strong cool (warm) SST anomalies in the eastern (western) Pacific
WSG-El Niño	1958–1959, 1968–1969 , 1976–1977, 1977–1978 , 1979–1980, 1986–1987 (6)	The warm (cool) SST anomalies in the eastern (western) Pacific but amplitude weaker than strong El Niño
WSG-La Niña	1971–1972, 1974–1975 , 2000–2001, 2008–2009 , 2011–2012 (5)	The same as WSG-El Niño but opposite in sign
Eq-El Niño	1963–1964 , 1969–1970, 1987–1988, 1994–1995 , 2002–2003, 2004–2005 , 2006–2007, 2014–2015 (8)	A significant zonal banded warming throughout the tropical oceans without a salient SST cooling in the western Pacific
Eq-La Niña	1964–1965, 1967–1968, 1971–1972, 1983–1984 , 1984–1985, 1985–1986, 1995–1996, 2005–2006 (8)	The same as Eq-El Niño but opposite in sign

Central-Pacific ENSO years are marked with bold fonts.

2. Materials and Methods

The merged Extended Reconstructed SST version 5 (ERSSTv5) [54] and the Hadley Centre Sea Ice and Sea Surface Temperature dataset (HadISST) [55] with the $2^\circ \times 2^\circ$ horizontal resolutions are used in this study. Atmospheric reanalysis datasets include ERA-40 [56] and ERA-Interim [57] data with a horizontal resolution of $1.5^\circ \times 1.5^\circ$. Precipitation Reconstruction (PREC) data were provided by NOAA [58]. The differences between the western Pacific K-shape and eastern Pacific triangle SSTs are defined by the mega-ENSO index [59]. The Niño-3.4 index is obtained from Climate Prediction Center (CPC). The NAO is defined using Hurrell’s station-based index [1]. The winter refers to the period from December to the next February. The data used for compositing analysis are de-trended to exclude the potential influence of linear trends.

We normalized the two ENSO indices to contrast them under the same criteria (Figure 1). The present study primarily employs composite analysis; the anomaly refers to the difference between the salient ENSO and ENSO-neutral years. “ENSO-neutral” indicates the normalized Niño3.4 index between -0.5 and 0.5 standard deviations (STD). ENSO events refer to the years with the absolute values of the Niño3.4 index greater than 0.5 STD. Considering that the average intensity of the selected warm and cold ENSO events is around ± 1.1 , we classify ENSO events as of weak intensity when the absolute value of the Niño3.4 index falls within 0.5 and 1.1 standard deviations and as strong intensity when the absolute value of the Niño3.4 index exceeds 1.1 . To separate strong and weak gradient ENSOs, we set ± 0.7 STD of the mega-ENSO index as the criteria. A strong gradient ENSO needs to satisfy the absolute value of the mega-ENSO index greater than 0.7 STD. If not, we define it as the weak gradient ENSO. Altering the criteria to ± 0.8 STD, the qualitative results will not change.

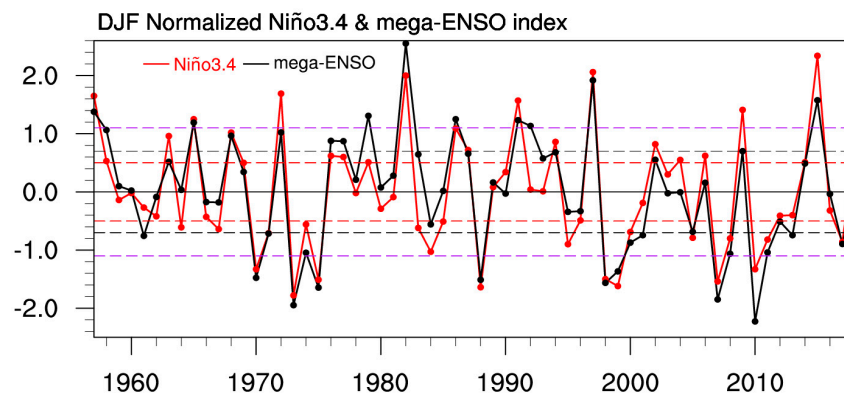


Figure 1. Time series of the normalized December–January–February (DJF) Niño3.4 (red curve) and mega-ENSO (black curve) indices for the period of 1957–2018. The mega-ENSO index is multiplied by -1 for comparison purposes. The red, black, and purple dashed lines denote ± 0.5 , ± 0.7 , and ± 1.1 , which refer to the thresholds for dividing ENSO events, SG/WG ENSO events, and strong/moderate ENSO events, respectively.

The European Center-Hamburg (ECHAM 5.4) [60] model from the Max Planck Institute is applied to illuminate a possible mechanism. The resolution is T63L19 (horizontal grid of 1.875° and 19 vertical levels). Forced by the observational AMIP II SST, the model was integrated from 1950 to 2010. To reduce the potential impact of ENSO, we picked out twenty neutral or weak ENSO winters from 1955 to 2010 as the samples for the control experiments. Next, sensitivity experiments consisted of nine groups of simulation. Each experiment was forced by climatological monthly mean SSTs (same as in the control run) and observed DJF SST anomalies. The initial conditions for the sensitivity simulations were acquired from the control run. The detailed experiment design is shown in Table 2.

Table 2. List of SST perturbation experiments conducted in this study.

Experiments	Description of SST Perturbation
SEN	SSTA associated with strong El Niño events is imposed in the Pacific (40° S– 40° N, 120° E– 90° W)
WSGEN	SSTA associated with strong gradient weak El Niño events is imposed in the tropical Pacific (40° S– 40° N, 120° E– 90° W)
EqEN	SSTA associated with weak gradient weak El Niño events is imposed in the tropical Pacific (15° S– 15° N, 160° E– 90° W)
IO	SSTA associated with strong El Niño events is imposed in the Indian Ocean (20° S– 20° N, 40° E– 110° E)
SEN_IO	SEN and IO SSTA forcings are added together
EqEN_IO	SSTA associated with weak gradient weak El Niño events is imposed in the tropical Pacific (20° S– 20° N, 160° E– 90° W) and Indian Ocean (20° S– 20° N, 40° E– 110° E)
SGLN	SSTA associated with strong gradient (strong and strong gradient weak) La Niña events is imposed in the tropical Pacific (40° S– 40° N, 120° E– 120° W)
WSGLN	SSTA associated with strong gradient weak La Niña events is imposed in the tropical Pacific (40° S– 40° N, 120° E– 120° W)
EqLN	SSTA associated with weak gradient weak La Niña events is imposed in the tropical Pacific (15° S– 15° N, 150° E– 90° W)

3. Results

3.1. Comparison of Different Types of ENSO and Related NAO

3.1.1. SSTA Patterns and Their Associated Tropic Atmospheric Responses

First, since the mega-ENSO index can well represent the strong and weak gradient ENSOs, combined with the Niño3.4 index, the ENSO events with different intensities and gradients might be distinguished. According to the method displayed in Section 2, three types of El Niño and three types of La Niña are classified (Table 1). Interestingly, the strong ENSOs commonly contain a sizeable zonal gradient; only the weak ENSOs can be

separated based on the east-west gradient to the weak intensity-strong gradient (WSG) and weak intensity-weak gradient events. Since the weak intensity-weak gradient events are confined in the equatorial region, they are labeled as equatorial (Eq) ENSO. Previous studies subdivided ENSO into the CP and EP groups according to the shift of the maximum SSTA [24,25,61,62]. Therefore, the CP ENSOs are bolded in Table 1, showing that the CP events occur randomly in the three flavors of El Niño; however, they coincide with the strong gradient (SG) La Niña, which consists of the strong and WSG La Niña.

Figure 2 compares the large-scale SST anomalies for the El Niño and La Niña types. Generally speaking, the spatial patterns are well classified. In the strong El Niño (SEN) winters, the obvious warm SSTAs dominate the eastern Pacific and Indian Ocean (IO), while the cold SSTAs appear in the western Pacific (Figure 2a). The strong La Niña (SLN) displays an SSTA distribution opposite to the SEN (Figure 2d). The WSG event also displays a Pacific “seesaw” pattern but a neutral IO SSTA (Figure 2b,e). In contrast, a salient narrow positive (negative) SSTA controls the equatorial central and eastern Pacific for the equatorial EN (equatorial LN) with significant warm (cold) SSTA in the IO (western IO) (Figure 2c,f). In addition, as shown in Table 1, several equatorial (SG) La Niña events coincide with the years of EP (CP) La Niña. Their spatial patterns show the maximum negative SSTA center in the tropical CP for SGLN (Figure 2d,e) but in the tropical EP for equatorial LN (Figure 2f). However, the centers of maximum SST anomalies shifted very little for the three types of El Niño (Figure 2a–c).

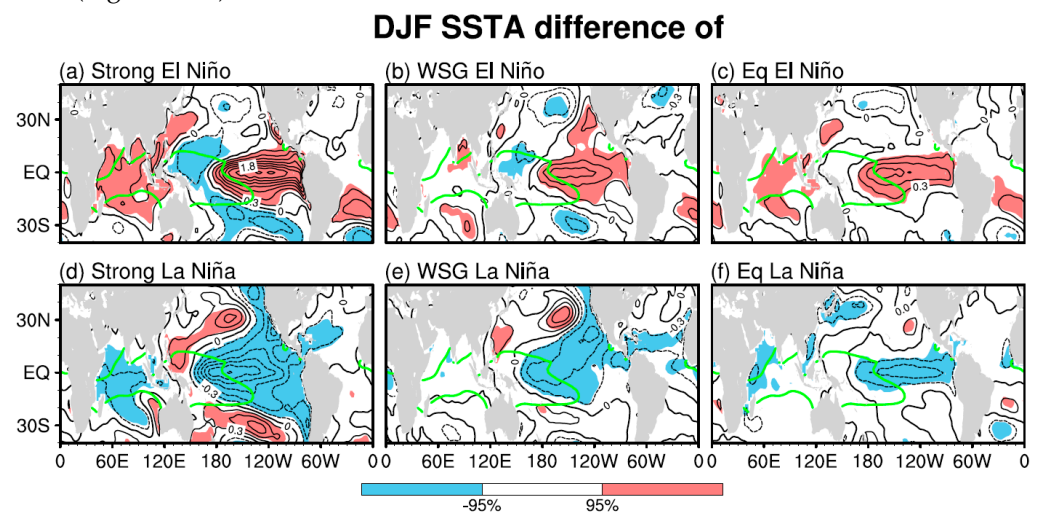


Figure 2. DJF sea surface temperature (SST; K, interval: 0.3 K) composite differences of (a) strong El Niño, (b) weak intensity-strong gradient (WSG) El Niño, and (c) equatorial (Eq) El Niño. (d–f) same as (a–c), but for La Niña events. The shadings in each panel represent the region with anomalies significant at the 95% confidence level (Student’s *t*-test). The green contour represents 28 °C isotherm.

Due to the diversity in ENSO intensity and spatial patterns, the precipitation anomalies associated with the different ENSOs exhibit distinct features (Figure 3). The tropical precipitation anomalies are stronger in response to intense ENSOs than weak events. For El Niños, the salient positive precipitation anomalies straddle the dateline with the negative anomalies controlling the western Pacific (WP) (Figure 3a–c). Significant discrepancies are found over the IO region with rich tropical rainfall generated by the warm local SSTA during the SEN and equatorial EN winters. However, no salient precipitation anomalies are seen in the WSGEN winters. For the La Niña events (Figure 3d–f), the neutral precipitation anomalies over the IO indicate a relatively weak local air-sea interaction compared to those of the SEN and WSGEN. It also shows the poor precipitation centers in the tropical central Pacific for the two SGLN cases but extends eastward during equatorial LN, which is attributed to the shift of the maximum center of SSTA.

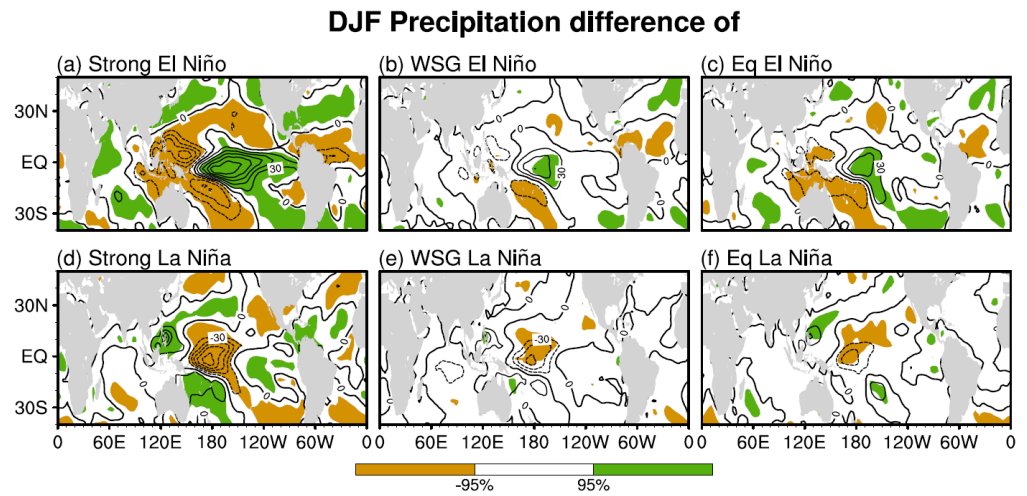


Figure 3. The same as Figure 2, except for tropical precipitation (mm/mon, interval: 30 mm/mon).

3.1.2. Unsteady Relationship of the ENSO with NAO

Next, we display the scatterplot of NAO and Niño3.4 indices in winter (Figure 4), and a complex relationship is detected between ENSO and NAO events. It shows that six WSGENs emerge with a negative NAO; however, the negative or positive NAO occurrence is evenly balanced during the SEN and equatorial EN winters, indicating a steady relationship between the NAO signal and the WSGEN. For the La Niña events, most of the SLN (6 of 8) and WSGLN (4 of 5) events, in other words, 10 of 13 SGLNs, are accompanied by a positive phase of NAO, but such relationships cannot be seen in the equatorial LN cases.

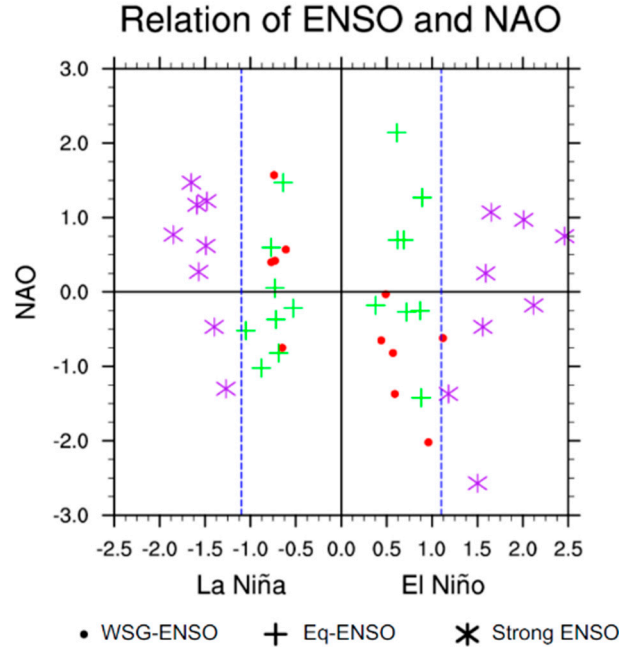


Figure 4. Scatter map of the DJF Niño3.4 and NAO indices for WSG-ENSO (red dots), equatorial ENSO (green crosses), and strong ENSO (purple snowflakes). The blue dashed line denotes ± 1.1 .

Figure 5 displays the anomalous 850-hPa geopotential height (Z850) and zonal wind at 200-hPa (U200) associated with the different types of ENSO to further inspect the extratropical atmospheric responses. During the EN winters (Figure 5a–c), anomalous positive SST in the tropical central and eastern Pacific induces salient diabatic heating, generating a large-scale Rossby wave train that resembles the PNA teleconnection pattern over the North Pacific (NP) and North America regions. Significant discrepancies are observed

over the NP as well as the North Atlantic. Over the NP region, although the apparent negative anomalies, which imply the enhanced Aleutian Low (AL), are seen in the three EN cases, they exhibit different intensities and spatial locations. Generally, the negative Z850 anomalies over NP for SEN (Figure 5a) are much stronger than the weak events (Figure 5b,c). Compared with the SEN and equatorial EN composites (Figure 5a,c), the enhanced AL associated with WSGEN moves eastward to some extent (Figure 5b). Over the North Atlantic, the Z850 anomalies for WSGEN (Figure 5b) exhibit a negative NAO-like anomaly with negative and positive centers over the Azores Island and Iceland, respectively. However, such an anomalous pattern over the North Atlantic cannot be seen in the SEN and equatorial EN cases (Figure 5a,c). For the LN cases, the Z850 anomalies feature a decreased AL over NP in the SGLN winters (Figure 5d). Simultaneously, negative and positive Z850 anomalies are evident in Iceland and Azores Island, respectively, reflecting a positive phase of NAO-like anomalies pattern. In contrast, the equatorial LN-related anomalous Z850 field (Figure 5e) displays the salient negative anomalies over the subtropical North Pacific, representing the southward movement of the AL. Meanwhile, the positive Z850 anomalies, instead of the NAO-like pattern, dominate the mid- to high-latitude North Atlantic.

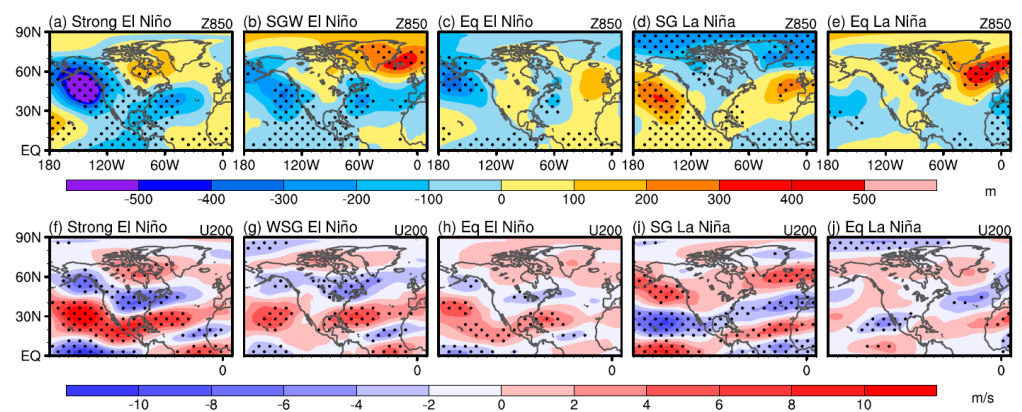


Figure 5. DJF 850-hPa geopotential height (Z850; m) composite differences of (a) strong El Niño—neutral, (b) WSG-El Niño—neutral, (c) Eq-El Niño—neutral, (d) SG-La Niña—neutral, and (e) Eq-La Niña—neutral. (f–j) same as (a–e) but for zonal wind at 200-hPa (U200; m/s). The dots in each panel represent the region with anomalies significant at the 90% confidence level (Student’s *t*-test).

We observed that only WSGENs, rather than the SEN and equatorial EN, are concurrent with a negative phase of the NAO event, indicating that both the change of intensity and east-west gradient in SST determine the linking of El Niño and NAO. For the La Niña cases, although the SLN and WSGLN display different amplitudes, they both show an obvious east-west gradient in SST. They are accompanied by a positive phase of NAO, which cannot be seen during the equatorial LN winter. Therefore, the influence of LN events on NAO mainly depends on the spatial distribution rather than the intensity of ENSO. We also noticed that compared to the equatorial LN events, the SSTA of SLN and WSGLN show strong east-west gradients, and the maximum negative values center in the equatorial CP. We, therefore, combine the SLN and WSGLN into one category, namely, the SGLN, and discuss the potential mechanisms for the impact of the WSGEN and SGLN on NAO in the next section.

3.1.3. Possible Mechanisms for the Impact of WSGEN and SGLN on NAO

The previous study [25] argued that the jet streams commonly act as an atmospheric bridge, transporting ENSO-induced planetary wave energy to the downstream region and resulting in an oscillation of the remote atmosphere, for instance, the air mass over the North Atlantic. The lower panel of Figure 5 displays the composite U200 anomalies in each ENSO winter.

In the El Niño cases, anomalous U200 displays the tripolar pattern in the NP and extends eastward of a different degree to the North Atlantic (Figure 5f–h). The intensified subtropical jet stream and the weakened mid-latitude westerly jet over North Atlantic tend to elongate farther eastward during the WSGEN winters (Figure 5g) than during the SEN and the equatorial El Niño winters (Figure 5f,h). Such a phenomenon implies that the two branches of westerly jets may serve as the “bridge” connecting the WSGEN and the negative phase of the NAO signal. However, this “bridge” effect is invalid for SEN and equatorial El Niño. For the La Niña events, an opposite situation is observed for the SGLN cases over the North Pacific–North Atlantic sector with the negative and positive U200 anomalies over the subtropical and mid-latitude North Atlantic, indicating the weakened subtropical and the enhanced mid-latitude jets, respectively (Figure 5i). In contrast, the equatorial La Niña-related U200 anomalies show a weakened and northeastward tilted westerly jet from the subtropical North Pacific extent far east to the Barents Sea, but without the salient tripolar structure over the North Pacific region and the dipolar anomalies over the North Atlantic (Figure 5j).

Numerical experiments were performed to identify the potential effects of westerly jets on connecting the tropical SSTAs corresponding to diverse ENSOs and NAO signals. The detailed experiment designs are listed in Table 2. Figure 6 displays the abnormal tropical precipitation, Z850, and U200 response to the SEN_IO, WSGEN, EqEN_IO, SGLN, and EqLN SSTAs forcing versus the CTRL run. In general, the simulated results can well reproduce the observational analysis counterparts. In the EN-type simulations, the prescribed warm SSTA in EP and IO with the cold SSTA in WP for the SEN_IO simulation leads to stronger tropical precipitation responses (Figure 6a) than those of the WSGEN (Figure 6b) and EqEN_IO (Figure 6c) experiments. Additionally, significant positive precipitation anomalies dominate tropical IO in the SEN_IO (Figure 6a) and EqEN_IO (Figure 6c) experiments but disappear in the WSGEN (Figure 6b) experiments. Further inspecting the Z850 responses to each EN-type SSTA forcing can reveal an enhanced AL over the NP in each anomalous Z850 field (Figure 6f–h). Over the North Atlantic region, the WSGEN SSTA forcing (Figure 6g) tends to induce a negative NAO anomaly, which cannot be seen in the SEN_IO (Figure 6f) and EqEN_IO (Figure 6h) simulations. In addition, the anomalous U200 exhibits a tripolar structure over the NP in each simulation (Figure 6k–m), and the salient discrepancies also appear over the North Atlantic region. The WSGEN SSTA forcing triggers the eastward spread of the subtropical and mid-latitude westerly jets (Figure 6l), confirming the observational result. In comparison, the two westerly jets cannot extend that far eastward, indicating the SEN_IO and EqEN_IO-types SSTAs are hard to trigger the NAO-like atmospheric anomaly through the “atmospheric bridge”—the westerly jets (Figure 6k,m).

In the two La Niña-type simulations, considering the weak air-sea interaction over the tropical IO region (Figure 3d–f), we imposed the SSTA associated with the SGLN and the equatorial LN mainly within the Pacific basin. The significant negative precipitation anomalies over the equatorial-CP and EP exhibit a much stronger intensity and extent more westward in response to the SGLN (Figure 6d) than to the EqLN forcing (Figure 6e). This may be due to the maximum SSTA centers straddling the equatorial CP for SGLN but in the equatorial-EP for equatorial LN. The resultant circulation fields for the SGLN simulation are contrary to that of the WSGEN simulation, showing a salient positive phase of NAO-like anomaly (Figure 6i) with the weakened subtropical westerly jet and the intensified mid-latitude jet (Figure 6n) over the North Atlantic. However, the Z850 and U200 responses over the North Atlantic exhibit a neutral pattern in the EqLN simulation (Figure 6j,o).

The above numerical experiments proved that the two branches of westerly jets serve as atmospheric bridges to extend the WSGEN/SGLN signals to the downstream regions, inducing NAO-like anomalies. However, why can the other types of ENSO SSTAs not expand their impact to the downstream North Atlantic?

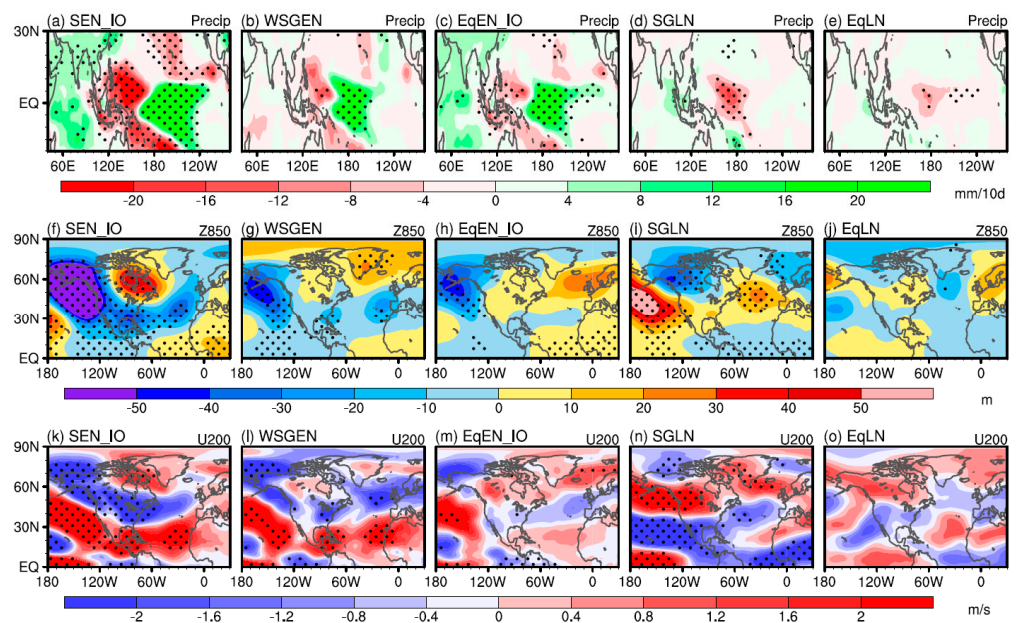


Figure 6. Tropical precipitation responses in the ECHAM5 regarding a difference between (a) SEN_IO, (b) WSGEN, (c) EqEN_IO, (d) SGLN, and (e) EqLN forcings and the control run (interval: 2 mm/month). (f–j) same as (a–e) but for geopotential at 850-hPa (Z850; 10 m). (k–o) same as (a–e) but for zonal wind at 200-hPa (U200; m/s). The dots represent the anomalies significant at the 90% confidence level (Student’s *t*-test).

3.1.4. The Causes for the Abruption of ENSO and NAO Relations

The observational and numerical analysis demonstrated that different El Niño/La Niña flavors exhibit intricate relations with the NAO phase. For the EN cases, we observed the salient positive SSTAs in the tropical IO for the SEN and equatorial EN cases (Figure 2a,c), reflecting the inter-basin coupling of the tropical Pacific and IO, which is the key to comprehending the teleconnection pathway on the globe that is rooted in the tropics [63–66]. Furthermore, the IO is also identified as a principal contributor to the North Atlantic extratropical atmospheric anomalies in winter [10,67,68]. Therefore, it is natural to speculate that the anomalous warm SST in the IO may modulate the linking of El Niño and NAO.

To verify our speculation, an IO warming (IOW) experiment was carried out with the positive SSTAs associated with SEN imposed onto the tropical IO, which induces rich local precipitation (Figure 7a) and a positive phase of NAO anomaly (Figure 7b). This atmosphere experiment confirms the previous studies that the slow variations of IO force the NAO on the seasonal time scale [67,69,70]. Next, the SEN and EqEN experiments were conducted without warm IO SSTA. The dipolar precipitation responses in the Pacific are much weaker in the EqEN simulation (Figure 7b) than in the SEN simulation (Figure 7c); both of them can trigger a negative NAO-like Z850 anomaly (Figure 7e,f). However, the NAO-like Z850 anomalies disappeared when the IO and SEN/EqEN forcings were imposed simultaneously (Figure 6f,h), indicating that the IO SSTA modulates the forcing of El Niño onto the NAO signals.

For the SGLN cases, the SSTA shows a sizeable east-west gradient with the maximum center in the equatorial CP (Figure 2d,e), generating a positive NAO-like anomaly over the North Atlantic (Figures 5d and 6i). By contrast, the equatorial LN features a weak east-west gradient with the maximum SSTA in the equatorial EP (Figure 2f), and the resultant atmospheric anomalies over the North Atlantic exhibit the NAO-neutral pattern (Figures 5e and 6j). However, although the amplitude of WSGEN (Figure 2e) is comparable with equatorial LN (Figure 2f) (their average intensities are -0.72 and -0.82 , respectively), their resultant precipitation anomalies exhibit significant discrepancies in

intensity (Figure 3e,f). Therefore, the differences in atmospheric anomalies associated with SGLN (Figure 5d) and equatorial LN (Figure 5e) may not depend on the amplitude of SSTA in the Niño3.4 region.

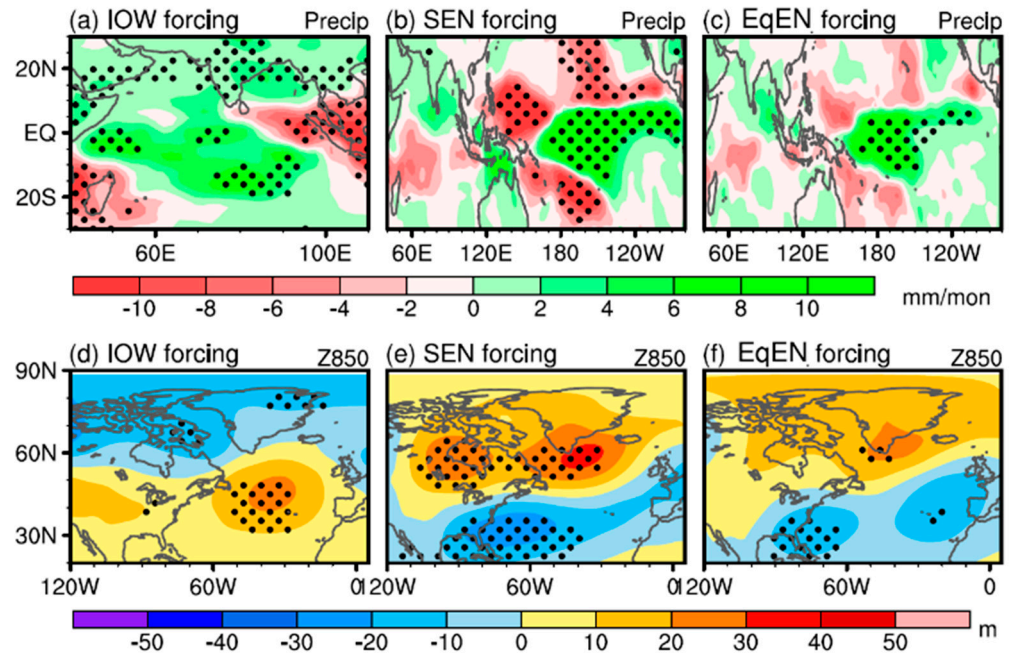


Figure 7. Tropical precipitation responses in the ECHAM5 regarding a difference between (a) IOW, (b) SEN, (c) EqEN forcings, and the control run (interval: 2 mm/month). (d–f) same as (a–c) but for geopotential at 850-hPa (Z850; 10 m). The dots represent the anomalies significant at the 90% confidence level (Student’s *t*-test).

Regarding the SSTA distributions, the SGLN and equatorial LN correspond to the CP and EP La Niñas, respectively. We know that the climatology SST, to a great extent, determines the occurrence of deep tropical convection; the threshold commonly is about 28 °C [71,72], and the variability of convection and atmospheric responses are primarily dependent on the anomalous tropical SST. Owing to the proximity of the central Pacific to the western Pacific warm pool, the climatology SSTs above 28 °C (green contours in Figure 2), abnormal convective motions, and extra-tropical atmospheric circulation usually present a quasi-linear response to SST anomalies [25]. During the SGLN winter, the negative SSTA in the CP superimposes on the climatology SST, significantly dropping local SST below 28 °C, reducing the deep convection and precipitation over the CP (Figure 3d,e). As a result, a steady forcing of SGLN on the atmospheric anomalies over the North Atlantic is established. In comparison, the low climatological SSTs normally do not reach the threshold to generate convection in the eastern Pacific. Consequently, the negative SSTAs in EP exert a weaker influence on the tropical convective motions and precipitation in the equatorial LN cases (Figure 3f). Therefore, changes in the maximum SSTA center in the tropical Pacific profoundly alter global teleconnections [38,73]. We further executed the WSGLN simulations with the associated SSTA imposed onto the Pacific region. Figure 8a displays the tropical precipitation anomalies in response to the WSGLN forcing versus CTRL run. The negative precipitation anomalies induced by WSGLN are concentrated in the tropical CP with rich rainfall over the WP. The large precipitation differences between WSGLN and EqLN simulations are seen over the tropical CP and EP (Figure 8b). The anomalous dipole mode over the Pacific indicates that WSGLN-type SSTA tends to reduce the tropical convection, weakening the convective motion more pronouncedly over the CP than the EP. The resultant Z850 anomalies for WSGLN forcing also highly resemble a positive phase of the NAO pattern (Figure 8c).

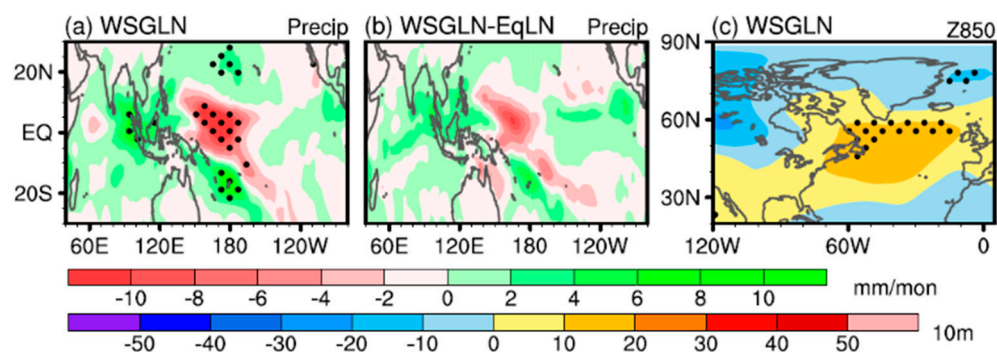


Figure 8. Tropical precipitation responses in the ECHAM5 regarding a difference between (a) WSGLN and the control run, (b) WSGLN and EqLN (interval: 2 mm/month), (c) same as (a) but for geopotential at 850-hPa (Z850; 10 m). The dots represent the anomalies significant at the 90% confidence level (Student's *t*-test).

4. Discussion

In the present work, we separated the different flavors of ENSO, but their physical backgrounds are unclear. Due to the limited space of this article, we give a short discussion. Figure 9 displays the seasonal evolution of sea surface temperatures and surface wind anomalies for the three El Niño types. For SEN and equatorial EN during the springtime (Figure 9a,i), significant westerly wind anomalies prevail in the western Pacific. On the one hand, the westerlies induce the upwelling of the subsurface water in the WP, cooling down the local SST. Conversely, the westerlies blow the warm waters in the western Pacific warm-pool eastward, warming up the equatorial central-eastern Pacific. Such a process can continue to function from summer to winter (upper and lower panels of Figure 9). During the early summer, the cooling in the WP increases the zonal gradient between the North IO (NIO), generating tropical easterlies across the NIO (Figure 9b,j), slowing down the background westerlies and continuing the warm SSTA in the NIO (Figure 9c,k), leading to a positive Indian Ocean Dipole (IOD)-like SSTA pattern in the autumn (Figure 9d,l). However, the IOD decays rapidly thereafter, and SEN and equatorial EN continue to force the IO, inducing an Indian Ocean basin-wide warm SSTA in the ensuing winter [74] (Figure 2a,c).

The SEN and equatorial EN, however, show significant discrepancies in the northwestern Pacific (NWP). For the SEN case, the intense equatorial central-eastern Pacific warming excites a Rossby wave west of the equatorial central Pacific. Anomalous northeasterly flow from North Pacific (NP) down to the tropical WP, speeding up the trades over the western NP (WNP). The resulting wind speed—stronger in the extra-tropical and WNP—induces SSTA changes in the WNP via the Wind-Evaporation-SST (WES) feedback [75]: the structure exhibits a strong east-west gradient (Figure 9d). In the equatorial EN case, the anomalous NWP cooling reaches its maximum in the early summer (Figure 9k) and decays in the autumn (Figure 9i). The weak WNP cold SSTA, going against the local air-sea interaction process proposed by Wang et al. [17], restricts the formation of the WNP anticyclone to accelerate the trade wind and then feedback to the local SST via the WES mechanism.

Nevertheless, the WSGEN exhibits a gradual enhancement of the west-east gradient in SST over the Pacific. The initial SST warming occurs in the equatorial EP, and cooling emerges in the subtropical WP during the early summer, with the westerlies prevailing over the equatorial CP (Figure 9f). The westerly wind anomalies become stronger in the late summer and autumn with the enhancement of the west-east gradient in SST over the Pacific (Figure 9g,h), reflecting a Bjerknes positive feedback process [41]. Moreover, the initial cool SSTA in the South China Sea (SCS) moves eastward from spring to autumn. During the summertime, the deficiency of the salient cool SSTA in SCS restricts the easterlies penetrating NIO and the development of the IOD. We also noticed that the dominant wind and SST anomalies in the extra-tropical NP, which cannot be seen in the equatorial EN

cases, may contribute to the cooling of the WP. However, the origin of the circulation and SST anomalies in the NP during the WSGEN autumn call for further investigation.

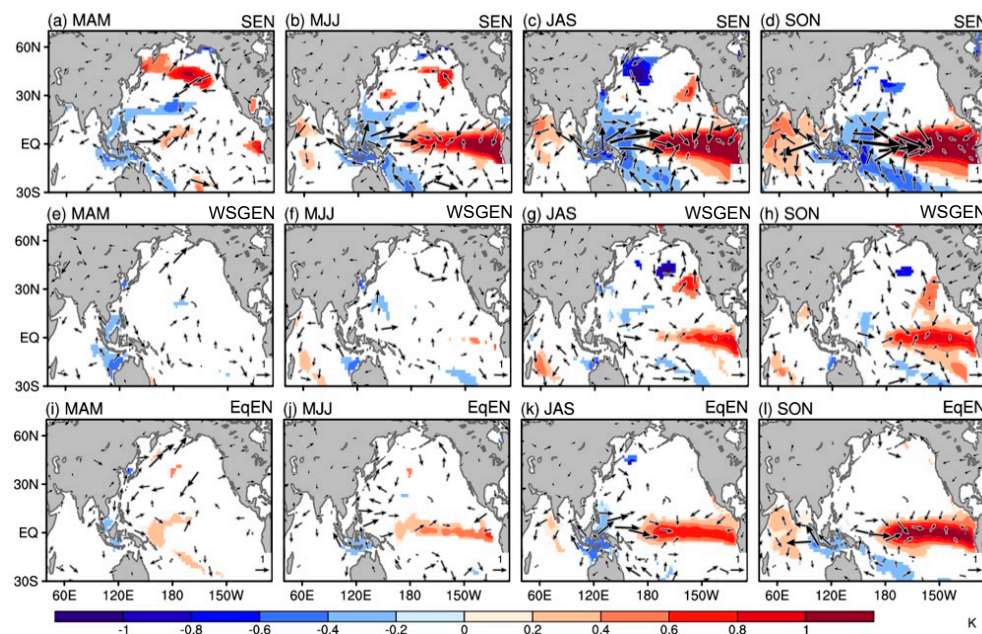


Figure 9. SST (internal: 0.2 K) and horizontal wind at 1000-hPa (UV1000; m/s) composite differences under strong El Niño. (a) March–April–May (MAM), (b) May–June–July (MJJ), (c) July–August–September (JAS), and (d) September–October–November (SON). (e–h) same as (a–d), but for WSG-El Niño. (i–l) for equatorial El Niño. The shadings and vectors in each panel represent the region with anomalies significant at the 90% confidence level (Student’s *t*-test).

For the La Niña events, the SGLN and equatorial LN coincide with the CP and EP La Niñas, respectively. Prior studies have revealed that the previous winter or spring North Pacific Oscillation (NPO) through seasonal footprint mechanism is largely responsible for triggering the CP ENSO [76–78]. Figure 10 shows the lead-lag composite of UV850 and SSTA for SGLN. An abnormal positive NPO-like pattern appears in the previous spring, driving the North Pacific SST and resulting in a tripolar SSTA pattern in the NP region (Figure 10a). Specifically, the anticyclonic anomalies occur over the subtropical to mid-latitude North Pacific, causing abnormal easterlies in the equatorial CP. The abnormal easterlies in the tropical CP induce convergence and give feedback to maintain the development of negative SSTAs (Figure 10b). Such an air-sea interaction process amplifies the equatorial zonal wind and SST anomalies, driving the evolution of La Niña from summer to autumn (Figure 10c,d). However, such a process cannot be seen for the equatorial LN (lower panel of Figure 10). It starts to develop in the late summer without the salient atmospheric signals. This oceanic process needs to be investigated.

We should also point out that dividing ENSOs based on intensity is still debatable. Alizadeh [79] grouped ENSOs into weak, moderate, strong, and very strong events. This classification is more elaborate but obtains smaller samples than our study does. Then, the unsupervised learning methods, such as clusters, self-organizing maps, and many others, should be examined to determine whether the different types of ENSO can be subdivided more objectively. Furthermore, we only apply the AGCM to mimic the various forcing effects of different types of ENSOs on the extra-tropical atmospheric anomalies. The lack of air-sea interaction process of AGCM makes it difficult to capture the potential effects of extra-tropical SSTAs (e.g., North Pacific), i.e., feedback to ENSO forcing, on the atmospheric anomalies over the North Atlantic. A better method would be to apply the samples of CMIP6 history experiments to verify our hypothesis.

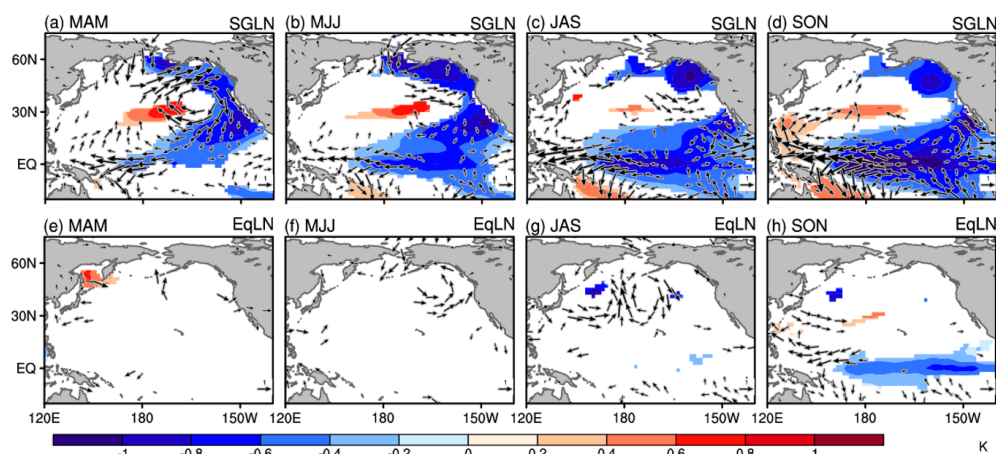


Figure 10. The same as Figure 9, but for SG-La Niña and equatorial La Niña.

5. Conclusions

The previous research pointed out that the combined effect of ENSO and NAO usually results in even more significant impacts than their individual effects [80,81]. It is, therefore, necessary to clarify their potential linkage. In this study, we classified the ENSO events according to their amplitude and east-west gradients in the Pacific. Strong ENSOs commonly contain a sizeable east-west gradient, and only the weak-intensity ENSOs can be separated based on the east-west gradient of the WSG and equatorial events. For the El Niño events, the SEN features a salient east-west gradient in the Pacific with the warming SST in the tropical IO (Figure 2a). The WSGEN also exhibits a strong gradient in the Pacific but without the significant warm SSTA in the IO (Figure 2b). The equatorial EN is characterized by the salient warm SSTA in the equatorial CP and EP, as well as in the tropical IO (Figure 2c). For the La Niña events, their spatial patterns in SST are roughly opposite to their EN counterparts (Figure 2d–f). In addition, the maximum SSTA for SLN and WSGLN centers in the equatorial CP but moves to the EP for the equatorial LN.

Next, we demonstrated that atmospheric anomalies in response to different ENSO types exhibit large discrepancies over the North Atlantic region (Figures 5 and 6). Only the WSGEN and SGLN events can produce NAO-like patterns through the eastward elongation of the two branches of the jet streams. During the WSGEN (SGLN) winter, the salient warm (cool) SSTA in the CP and EP and the opposite anomalies in the WP induce enhanced (weakened) subtropical and weakened (enhanced) mid-latitude westerly jets, leading to a negative (positive) NAO-like anomaly. By contrast, the NAO-like anomaly cannot be detected in other ENSO cases. The further study implied that the warm SSTA in the IO (Figure 7), which triggers abundant precipitation in the tropical IO during the SEN and equatorial EN winters, generates a positive NAO pattern that offsets the effect of El Niño signals in the Pacific region, inducing an NAO-neutral anomalies pattern. However, the IO SSTA cannot modulate the relation of LN and NAO owing to the weak forcing of the cool IO SSTA on local precipitation and remote teleconnections. The SGLN's maximum SSTA is located over the CP, where the climatology SST exceeds the threshold for exciting deep convective motion. The negative SSTA in the CP consistently influences atmospheric circulation, resulting in a response over the North Atlantic that resembles a positive NAO. In comparison, the maximum SSTA of equatorial LN centers in the EP, where the climatology SST is below the threshold for deep convection. The atmospheric response over the North Atlantic shows a neutral pattern.

This study further illustrates the important roles ENSO diversity plays in affecting atmospheric variability over remote regions, especially over the North Atlantic. The atmospheric/coupled general circulation model may offer better analysis for the seasonal prediction of the NAO when considering the ENSO diversity according to its amplitude and the zonal gradient in SST over the Pacific.

Other than the roles of the troposphere, tropical warming excites a poleward-propagating Rossby wave train, which can also extend upward and reach the stratosphere, resulting in a weaker polar vortex that drives a negative NAO anomaly over the NA–Eurasia. In subsequent studies, we would like to examine whether or not SG-ENSO can affect the NAO through stratospheric pathways. Moreover, we will try to classify the summertime ENSO events and inspect their potential forcing effects on extra-tropical atmospheric anomalies.

Author Contributions: Conceptualization, P.Z. and Z.W.; methodology, P.Z.; software, P.Z.; validation, P.Z. and Z.W.; formal analysis, P.Z.; investigation, Z.W.; resources, P.Z.; data curation, P.Z.; writing—original draft preparation, P.Z.; writing—review and editing, Z.W.; visualization, P.Z.; supervision, Z.W.; project administration, Z.W.; funding acquisition, Z.W. All authors have read and agreed to the published version of the manuscript.

Funding: This work is jointly supported by the National Natural Science Foundation of China (NSFC) (Grant Nos. 91937302) and the Ministry of Science and Technology of China (Grant Nos. 2019QZKK0102, 2019YFC1509100 and 2017YFC1502302).

Data Availability Statement: The ERA-40 and ERA-interim datasets identified and investigated in this study are provided by ECMWF websites: <https://www.ecmwf.int/en/forecasts/datasets/browse-reanalysis-datasets>; The SST data from: <https://psl.noaa.gov/data/gridded/data.noaa.ersst.v5.html> and <https://www.metoffice.gov.uk/hadobs/hadisst/data/download.html>; The precipitation data from: <https://psl.noaa.gov/data/gridded/data.prec.html>. The ERA-40 data is accessed on 1 June 2017, other datasets are accessed on 20 March 2020.

Conflicts of Interest: The authors declare no conflict of interest. The funders had no role in the design of the study; in the collection, analyses, or interpretation of data; in the writing of the manuscript; or in the decision to publish the results.

References

- Hurrell, J.W. Decadal Trends in the North Atlantic Oscillation: Regional Temperatures and Precipitation. *Science* **1995**, *269*, 676–679. [[CrossRef](#)] [[PubMed](#)]
- Thompson, D.W.; Wallace, J.M. The Arctic Oscillation signature in the wintertime geopotential height and temperature fields. *Geophys. Res. Lett.* **1998**, *25*, 1297–1300. [[CrossRef](#)]
- Li, J.; Wang, J. A new North Atlantic Oscillation index and its variability. *Adv. Atmos. Sci.* **2003**, *20*, 661–676.
- Deser, C.; Hurrell, J.W.; Phillips, A.S. The role of the North Atlantic Oscillation in European climate projections. *Clim. Dyn.* **2017**, *49*, 3141–3157. [[CrossRef](#)]
- Branstator, G.; Selten, F. “Modes of Variability” and Climate Change. *J. Clim.* **2009**, *22*, 2639–2658. [[CrossRef](#)]
- Hurrell, J.W.; Deser, C. North Atlantic climate variability: The role of the north atlantic oscillation. *J. Mar. Syst.* **2009**, *78*, 28–41. [[CrossRef](#)]
- Butler, A.H.; Polvani, L.M.; Deser, C. Separating the stratospheric and tropospheric pathways of El Niño–Southern Oscillation teleconnections. *Environ. Res. Lett.* **2014**, *9*, 024014. [[CrossRef](#)]
- Scaife, A.A.; Arribas, A.; Blockley, E.; Brookshaw, A.; Clark, R.T.; Dunstone, N.; Eade, R.; Fereday, D.; Folland, C.K.; Gordon, M.; et al. Skillful long-range prediction of European and North American winters. *Geophys. Res. Lett.* **2014**, *41*, 2514–2519. [[CrossRef](#)]
- Kidston, J.; Scaife, A.A.; Hardiman, S.C.; Mitchell, D.M.; Butchart, N.; Baldwin, M.P.; Gray, L.J. Stratospheric influence on tropospheric jet streams, storm tracks and surface weather. *Nat. Geosci.* **2015**, *8*, 433–440. [[CrossRef](#)]
- Hoerling, M.P.; Hurrell, J.W.; Xu, T.; Bates, G.T.; Phillips, A.S. Twentieth century north atlantic climate change. Part II. Understanding the effect of indian ocean warming. *Clim. Dyn.* **2004**, *23*, 391–405. [[CrossRef](#)]
- Bracco, A.; Kucharski, F.; Kallummal, R.; Molteni, F. Internal variability, external forcing and climate trends in multi-decadal AGCM ensembles. *Clim. Dyn.* **2004**, *23*, 659–678. [[CrossRef](#)]
- Li, Y.; Lau, N.C. Impact of ENSO in the atmospheric variability over the North Atlantic in late winter—Role of transient eddies. *J. Clim.* **2012**, *25*, 320–342. [[CrossRef](#)]
- Wyrtki, K. El Niño—The Dynamic Response of the Equatorial Pacific Ocean to Atmospheric Forcing. *J. Phys. Oceanogr.* **1975**, *5*, 572–584. [[CrossRef](#)]
- Qadimi, M.; Alizadeh, O.; Irannejad, P. Impacts of the El Niño–Southern Oscillation on the strength and duration of the Indian summer monsoon. *Meteorol. Atmos. Phys.* **2021**, *133*, 553–564. [[CrossRef](#)]
- Held, I.M.; Lyons, S.W.; Nigam, S. Transients and the extratropical response to El Niño. *J. Atmos. Sci.* **1989**, *46*, 163–174. [[CrossRef](#)]
- Alizadeh-Choobari, O.; Adibi, P.; Irannejad, P. Impact of the El Niño–Southern Oscillation on the climate of Iran using ERA-Interim data. *Clim. Dyn.* **2018**, *51*, 2897–2911. [[CrossRef](#)]
- Wang, B.; Wu, R.G.; Fu, X.H. Pacific–East Asia teleconnection: How does ENSO affect East Asian climate? *J. Clim.* **2000**, *13*, 1517–1536. [[CrossRef](#)]

18. Ropelewski, C.F.; Halpert, M.S. Global and regional scale precipitation patterns associated with the El Niño/Southern Oscillation. *Mon. Weather Rev.* **1987**, *115*, 1606–1626. [[CrossRef](#)]
19. Trenberth, K.E.; Caron, J.M. The Southern Oscillation revisited: Sea level pressure, surface temperatures, and precipitation. *J. Clim.* **2000**, *13*, 4358–4365. [[CrossRef](#)]
20. Merkel, U.; Latif, M. A high-resolution AGCM study of the El Niño impact on the North Atlantic/European sector. *Geophys. Res. Lett.* **2002**, *29*, 1291. [[CrossRef](#)]
21. Ineson, S.; Scaife, A.A. The role of the stratosphere in the European climate response to El Niño. *Nat. Geosci.* **2009**, *2*, 32–36. [[CrossRef](#)]
22. Jiménez-Esteve, B.; Domeisen, D.I.V. The Tropospheric Pathway of the ENSO–North Atlantic Teleconnection. *J. Clim.* **2018**, *31*, 4563–4584. [[CrossRef](#)]
23. Brönnimann, S. Impact of El Niño–Southern Oscillation on European climate. *Rev. Geophys.* **2007**, *45*, RG3003. [[CrossRef](#)]
24. Zhang, W.; Wang, L.; Xiang, B.Q.; Qi, L.; He, J. Impacts of two types of La Niña on the NAO during boreal winter. *Clim. Dyn.* **2015**, *44*, 1351–1366. [[CrossRef](#)]
25. Zhang, W.; Wang, Z.; Stuecker, M.F.; Turner, A.G.; Jin, A.G.; Geng, X. Impact of ENSO longitudinal position on teleconnections to the NAO. *Clim. Dyn.* **2019**, *2*, 257–274. [[CrossRef](#)]
26. Zhang, P.; Wang, B.; Wu, Z. Weak El Niño and winter climate in the mid-high latitude Eurasia. *J. Clim.* **2019**, *32*, 402–421. [[CrossRef](#)]
27. Zhang, P.; Wu, Z.; Li, J. Reexamining the relationship of La Niña and the east Asian winter monsoon. *Clim. Dyn.* **2019**, *53*, 779–791. [[CrossRef](#)]
28. Zhang, P.; Wu, Z. Reexamining the connection of El Niño and North American winter climate. *Int. J. Climatol.* **2021**, *41*, 6133–6144. [[CrossRef](#)]
29. Polvani, L.M.; Sun, L.; Butler, A.H.; Richter, J.H.; Deser, C. Distinguishing stratospheric sudden warmings from ENSO as key drivers of wintertime climate variability over the North Atlantic and Eurasia. *J. Clim.* **2017**, *30*, 1959–1969. [[CrossRef](#)]
30. Wu, Z.; Zhang, P. Interdecadal variability of the mega-ENSO–NAO synchronization in winter. *Clim. Dyn.* **2015**, *45*, 1117–1128. [[CrossRef](#)]
31. Capotondi, A.; Wittenberg, A.T.; Newman, M.; Di Lorenzo, E.; Yu, J.Y.; Braconnot, P.; Cole, J.; Dewitte, B.; Giese, B.; Guilyardi, E.; et al. Understanding ENSO diversity. *Bull. Am. Meteorol. Soc.* **2015**, *96*, 921–938. [[CrossRef](#)]
32. McPhaden, M.J. Genesis and evolution of the 1997–1998 El Niño. *Science* **1999**, *283*, 950–954. [[CrossRef](#)] [[PubMed](#)]
33. Jacox, M.G.; Hazen, E.L.; Zaba, K.D.; Rudnick, D.L.; Edwards, C.A.; Moore, A.M.; Bograd, S.J. Impacts of the 2015–2016 El Niño on the California current system: Early assessment and comparison to past events. *Geophys. Res. Lett.* **2016**, *43*, 7072–7080. [[CrossRef](#)]
34. Toniazzi, T.; Scaife, A.A. The influence of ENSO on winter North Atlantic climate. *Geophys. Res. Lett.* **2006**, *33*, L24704. [[CrossRef](#)]
35. Xue, F.; Liu, C. The influence of moderate ENSO on summer rainfall in eastern China and its comparison with strong ENSO. *Chin. Sci. Bull.* **2008**, *53*, 791–800. [[CrossRef](#)]
36. Alizadeh-Choobari, O.; Najafi, M.S. Climate variability in Iran in response to the diversity of the El Niño–Southern Oscillation. *Int. J. Climatol.* **2018**, *38*, 4239–4250. [[CrossRef](#)]
37. Kao, H.; Yu, J. Contrasting Eastern-Pacific and Central-Pacific Types of ENSO. *J. Clim.* **2009**, *22*, 615–632. [[CrossRef](#)]
38. Alizadeh-Choobari, O. Contrasting global teleconnection features of the eastern Pacific and central Pacific El Niño events. *Dyn. Atmos. Ocean* **2017**, *80*, 139–154. [[CrossRef](#)]
39. Feng, J.; Li, J.P.; Zheng, F.; Xie, F.; Sun, C. Contrasting impacts of developing phases of two types of El Niño on southern China rainfall. *J. Meteorol. Soc. Jpn.* **2016**, *94*, 359–370. [[CrossRef](#)]
40. Wang, B.; Luo, X.; Yang, Y.M.; Sun, W.; Cane, M.A.; Cai, W.; Yeh, S.W.; Liu, J. Historical change of El Niño properties sheds light on future changes of extreme El Niño. *Proc. Natl. Acad. Sci. USA* **2019**, *116*, 22512–22517. [[CrossRef](#)]
41. Bjerknes, J. Atmospheric teleconnections from the equatorial Pacific. *Mon. Weather Rev.* **1969**, *97*, 163–172. [[CrossRef](#)]
42. Hoell, A.; Funk, C. The ENSO-related West Pacific Sea surface temperature gradient. *J. Clim.* **2013**, *26*, 9545–9562. [[CrossRef](#)]
43. Liebmann, B.; Hoerling, M.P.; Funk, C.; Bladé, I.; Dole, R.M.; Allured, D.; Quan, X.; Pegion, P.; Eischeid, J.K. Understanding recent eastern horn of Africa rainfall variability and change. *J. Clim.* **2014**, *27*, 8630–8645. [[CrossRef](#)]
44. Zinke, J.; Hoell, A.; Lough, J.M.; Feng, M.; Kuret, A.J.; Clarke, H.; Ricca, V.; Rankenburg, K.; McCulloch, M.T. Coral record of Southeast Indian Ocean marine heatwaves with intensified Western Pacific temperature gradient. *Nat. Commun.* **2015**, *6*, 8562. [[CrossRef](#)] [[PubMed](#)]
45. Zhang, L.; Wu, Z.; Zhou, Y. Different impacts of typical and atypical ENSO on the Indian summer rainfall: ENSO developing phase. *Atmos. Ocean* **2016**, *54*, 440–456. [[CrossRef](#)]
46. Meinen, C.S.; McPhaden, M.J. Observations of Warm Water Volume Changes in the Equatorial Pacific and Their Relationship to El Niño and La Niña. *J. Clim.* **2000**, *13*, 3551–3559. [[CrossRef](#)]
47. Jin, F.-F.; An, S.; Timmermann, A.; Zhao, J. Strong El Niño Events and Nonlinear Dynamical Heating. *Geophys. Res. Lett.* **2003**, *30*, 1120. [[CrossRef](#)]
48. An, S.-I.; Jin, F.-F. Why El Niño is Stronger than La Niña. *J. Clim.* **2004**, *17*, 2399–2412. [[CrossRef](#)]
49. Larkin, N.K.; Harrison, D.E. ENSO warm (El Niño) and cold (La Niña) event life cycles: Ocean surface anomaly patterns, their symmetries, asymmetries, and implications. *J. Clim.* **2002**, *15*, 1118–1140. [[CrossRef](#)]

50. Okumura, Y.M.; Deser, C. Asymmetry in the duration of El Niño and La Niña. *J. Clim.* **2010**, *23*, 5826–5843. [[CrossRef](#)]
51. Chen, M.; Li, T. ENSO evolution asymmetry: EP versus CP El Niño. *Clim. Dyn.* **2021**, *56*, 3569–3579. [[CrossRef](#)]
52. Zhang, R.; Li, T.-R.; Wen, M.; Liu, L.-K. Role of intraseasonal oscillation in asymmetric impacts of El Niño and La Niña on the rainfall over southern China in boreal winter. *Clim. Dyn.* **2015**, *45*, 559–567. [[CrossRef](#)]
53. Song, X.; Zhang, R.; Rong, X. Influence of intraseasonal oscillation on the asymmetric decays of El Niño and La Niña. *Adv. Atmos. Sci.* **2019**, *36*, 779–792. [[CrossRef](#)]
54. Huang, B.; Thorne, P.W.; Banzon, V.F.; Boyer, T.; Chepurin, G.; Lawrimore, J.H.; Menne, M.J.; Smith, T.M.; Vose, R.S.; Zhang, H.M. Extended reconstructed sea surface temperature, version 5 (ERSSTv5): Upgrades, validations, and intercomparisons. *J. Clim.* **2017**, *30*, 8179–8205. [[CrossRef](#)]
55. Rayner, N.A.; Parker, D.E.; Horton, E.B.; Folland, C.K.; Alexander, L.V.; Rowell, D.P.; Kent, E.C.; Kaplan, A. Global analyses of sea surface temperature, sea ice, and night marine air temperatures since the late nineteenth century. *J. Geophys. Res.* **2003**, *108*, 4407. [[CrossRef](#)]
56. Uppala, S.M.; Kållberg, P.W.; Simmons, A.J.; Andrae, U.; Bechtold, V.D., C.; Fiorino, M.; Gibson, J.K.; Haseler, J.; Hernandez, A.; Kelly, G.A.; et al. The ERA-40 re-analysis. *Q. J. R. Meteorol. Soc.* **2005**, *131*, 2961–3012. [[CrossRef](#)]
57. Dee, D.P.; Uppala, S.M.; Simmons, A.J.; Berrisford, P.; Poli, P.; Kobayashi, S.; Andrae, U.; Balmaseda, M.A.; Balsamo, G.; Bauer, D.P.; et al. The ERA-Interim reanalysis: Configuration and performance of the data assimilation system. *Q. J. R. Meteorol. Soc.* **2011**, *137*, 553–597. [[CrossRef](#)]
58. Chen, M.; Xie, P.; Janowiak, J.; Arkin, P.A. Global land precipitation: A 50-yr analysis based on gauge observations. *J. Hydrometeorol.* **2002**, *3*, 249–266. [[CrossRef](#)]
59. Wang, B.; Liu, J.; Kim, H.J.; Webster, P.J.; Yim, S.Y.; Xiang, B.Q. Northern Hemisphere summer monsoon intensified by mega-El Niño/southern oscillation and Atlantic multidecadal oscillation. *Proc. Natl. Acad. Sci. USA* **2013**, *110*, 5347–5352. [[CrossRef](#)]
60. Roeckner, E.; Bäuml, G.; Bonaventura, L.; Brokopf, R.; Esch, M.; Giorgetta, M.; Hagemann, S.; Kirchner, I.; Kornblueh, L.; Manzini, E.; et al. The atmospheric general circulation model ECHAM5. Part I: Model description. *Max Planck Inst. Rep.* **2003**, *349*, 140.
61. Ashok, K.; Behera, S.; Rao, A.S.; Weng, H.Y.; Yamagata, T. El Niño Modoki and its possible teleconnection. *J. Geophys. Res.* **2007**, *112*, C11007. [[CrossRef](#)]
62. Graf, H.-F.; Zanchettin, D. Central Pacific El Niño, the ‘subtropical bridge,’ and Eurasian climate. *J. Geophys. Res.* **2012**, *117*, D01102. [[CrossRef](#)]
63. Saji, N.H.; Yamagata, T. Structure of SST and surface wind variability during Indian Ocean dipole mode events: COADS observations. *J. Clim.* **2003**, *16*, 2735–2751. [[CrossRef](#)]
64. Luo, J.-J.; Zhang, R.; Behera, S.K.; Masumoto, Y.; Jin, F.-F.; Lukas, R.; Yamagata, T. Interaction between El Niño and extreme Indian Ocean dipole. *J. Clim.* **2010**, *23*, 726–742. [[CrossRef](#)]
65. Cai, W.; van Rensch, P.; Cowan, T.; Hendon, H.H. An asymmetry in the IOD and ENSO teleconnection pathway and its impact on Australian climate. *J. Clim.* **2012**, *25*, 6318–6329. [[CrossRef](#)]
66. Ha, K.J.; Chu, J.E.; Lee, J.Y.; Yun, K.S. Interbasin coupling between the tropical Indian and Pacific Ocean on interannual timescale: Observation and CMIP5 reproduction. *Clim. Dyn.* **2017**, *48*, 459–475. [[CrossRef](#)]
67. Bader, J.; Latif, M. North Atlantic Oscillation response to anomalous Indian Ocean SST in a coupled GCM. *J. Clim.* **2005**, *18*, 5382–5389. [[CrossRef](#)]
68. Lin, H.; Brunet, G.; Derome, J. An observed connection between the North Atlantic Oscillation and the Madden-Julian Oscillation. *J. Clim.* **2009**, *22*, 364–380. [[CrossRef](#)]
69. Bader, J.; Latif, M. The impact of decadal-scale Indian Ocean sea surface temperature anomalies on Sahelian rainfall and the North Atlantic Oscillation. *Geophys. Res. Lett.* **2003**, *30*, 2169. [[CrossRef](#)]
70. Hurrell, J.W.; Hoerling, M.P.; Phillips, A.; Xu, T. Twentieth century North Atlantic climate change. Part I: Assessing determinism. *Clim. Dyn.* **2004**, *23*, 371–389. [[CrossRef](#)]
71. Graham, N.E.; Barnett, T.P. Sea surface temperature, surface wind divergence, and convection over tropical oceans. *Science* **1987**, *238*, 657–659. [[CrossRef](#)] [[PubMed](#)]
72. Lau, K.-M.; Wu, H.T.; Bony, S. The Role of Large-Scale Atmospheric Circulation in the Relationship between Tropical Convection and Sea Surface Temperature. *J. Clim.* **1997**, *10*, 381–392. [[CrossRef](#)]
73. Domeisen, D.I.; Garfinkel, C.I.; Butler, A.H. The teleconnection of El Niño Southern Oscillation to the stratosphere. *Rev. Geophys.* **2019**, *57*, 5–47. [[CrossRef](#)]
74. Du, Y.; Xie, S.-P.; Hu, K.; Huang, G. Role of air–sea interaction in the long persistence of El Niño–induced North Indian Ocean warming. *J. Clim.* **2009**, *22*, 2023–2038. [[CrossRef](#)]
75. Xie, S.-P. The Shape of Continents, Air-Sea Interaction, and the Rising Branch of the Hadley Circulation. In *The Hadley Circulation: Past, Present and Future*; Diaz, H., Bradley, R.S., Eds.; Kluwer Academic: Amsterdam, The Netherlands, 2004; pp. 121–152.
76. Vimont, D.J.; Alexander, M.A.; Newman, M. Optimal growth of Central and East Pacific ENSO events. *Geophys. Res. Lett.* **2014**, *41*, 4027–4034. [[CrossRef](#)]
77. Yu, J.-Y.; Kao, H.Y.; Lee, T. Subtropics-Related Interannual Sea Surface Temperature Variability in the Equatorial Central Pacific. *J. Clim.* **2010**, *23*, 2869–2884. [[CrossRef](#)]
78. Yu, J.-Y.; Paek, H. Precursors of ENSO beyond the tropical Pacific. *US CLIVAR Var.* **2015**, *13*, 15–20.

79. Alizadeh, O. Amplitude, duration, variability, and seasonal frequency analysis of the El Niño-Southern Oscillation. *Clim. Chang.* **2022**, *174*, 20. [[CrossRef](#)]
80. Wu, Z.; Lin, H. Interdecadal variability of the ENSO-North Atlantic Oscillation connection in boreal summer. *Q. J. R. Meteorol. Soc.* **2012**, *138*, 1668–1675. [[CrossRef](#)]
81. Seager, R.; Kushnir, Y.; Nakamura, J.; Ting, M.; Naik, N. Northern Hemisphere winter snow anomalies: ENSO, NAO and the winter of 2009/10. *Geophys. Res. Lett.* **2010**, *37*, L14703. [[CrossRef](#)]

Disclaimer/Publisher’s Note: The statements, opinions and data contained in all publications are solely those of the individual author(s) and contributor(s) and not of MDPI and/or the editor(s). MDPI and/or the editor(s) disclaim responsibility for any injury to people or property resulting from any ideas, methods, instructions or products referred to in the content.